


# Effect of sample temperature on femtosecond laser ablation of copper

Wei-Jie Dang(党伟杰), Yu-Tong Chen(陈雨桐), An-Min Chen(陈安民), and Ming-Xing Jin(金明星)
**Citation:**Chin. Phys. B, 2024, 33 (**2**): 024207. DOI: 10.1088/1674-1056/ad028f
Journal homepage: http://cpb.iphy.ac.cn; http://iopscience.iop.org/cpb

**What follows is a list of articles you may be interested in**

---

## High power supercontinuum generation by dual-color femtosecond laser pulses in fused silica

Saba Zafar, Dong-Wei Li(李东伟), Acner Camino, Jun-Wei Chang(常峻巍), and Zuo-Qiang Hao(郝作强)
Chin. Phys. B, 2022, 31 (**8**): 084209. DOI: 10.1088/1674-1056/ac46be

## Wavelength and sensitivity tunable long period gratings fabricated in fluid-cladding microfibers

Wa Jin(金娃), Linke Zhang(张林克), Xiang Zhang(张祥), Ming Xu(徐铭), Weihong Bi(毕卫红), and Yuefeng Qi(齐跃峰)
Chin. Phys. B, 2022, 31 (**1**): 014207. DOI: 10.1088/1674-1056/ac3394

## Generation of wideband tunable femtosecond laser based on nonlinear propagation of power-scaled mode-locked femtosecond laser pulses in photonic crystal fiber

Zhiguo Lv(吕志国) and Hao Teng(滕浩)
Chin. Phys. B, 2021, 30 (**4**): 044209. DOI: 10.1088/1674-1056/abe231

## Effect of recombination process in femtosecond laser-induced modification on Ge crystal

Jia-Qi Ju(居家奇), Zi-Yao Qin(秦子尧), Ju-Kun Liu(刘聚坤), Hong-Wei Zhao(赵宏伟), Yao-Qing Huang(黄耀清), Rong-Rong Hu(胡蓉蓉), and Hua Wu(吴华)$
Chin. Phys. B, 2020, 29 (**11**): 114208. DOI: 10.1088/1674-1056/abbbe9

## Excitation-wavelength-dependent THz wave modulation via external bias electric field

Shi-Jia Feng(冯世嘉), Li-Quan Dong(董立泉), Dan-Ni Ma(马丹妮), Tong Wu(吴同), Yong Tan(谭永), Liang-Liang Zhang(张亮亮), Cun-Lin Zhang(张存林), Yue-Jin Zhao(赵跃进)
Chin. Phys. B, 2020, 29 (**6**): 064210. DOI: 10.1088/1674-1056/ab84d7

---

# Effect of sample temperature on femtosecond laser ablation of copper

Wei-Jie Dang(党伟杰)[1,2], Yu-Tong Chen(陈雨桐)[1,2], An-Min Chen(陈安民)[1,2,†], and Ming-Xing Jin(金明星)[1,2,‡]

[1] *Institute of Atomic and Molecular Physics, Jilin University, Changchun* 130012, *China*

[2] *Jilin Provincial Key Laboratory of Applied Atomic and Molecular Spectroscopy, Jilin University, Changchun* 130012, *China*

(Received 18 July 2023; revised manuscript received 11 October 2023; accepted manuscript online 12 October 2023)

We conduct an experimental study supported by theoretical analysis of single laser ablating copper to investigate the interactions between laser and material at different sample temperatures, and predict the changes of ablation morphology and lattice temperature. For investigating the effect of sample temperature on femtosecond laser processing, we conduct experiments on and simulate the thermal behavior of femtosecond laser irradiating copper by using a two-temperature model. The simulation results show that both electron peak temperature and the relaxation time needed to reach equilibrium increase as initial sample temperature rises. When the sample temperature rises from 300 K to 600 K, the maximum lattice temperature of the copper surface increases by about 6500 K under femtosecond laser irradiation, and the ablation depth increases by 20%. The simulated ablation depths follow the same general trend as the experimental values. This work provides some theoretical basis and technical support for developing femtosecond laser processing in the field of metal materials.

**Keywords:** femtosecond laser, two-temperature model, sample temperature, ablation depth

**PACS:** 42.62.–b, 52.38.Mf **DOI:** 10.1088/1674-1056/ad028f

## 1. Introduction

Laser is a new type of processing tool. It does not use sharp blades to cut and destroy materials like traditional tools. It involves complex physical and chemical processes.[1–3] Pulse laser has the characteristics of short action time, high processing accuracy, and a wide range of processing materials. It is widely used in various fields such as microfabrication, healthcare, and aerospace.[4–7] Researchers often use nanosecond laser pulses to process materials and have developed some methods to improve the laser ablation rate, such as double-pulse laser ablation of materials,[8,9] adding magnetic fields near the samples,[10,11] and preheating the samples.[12,13] Increasing the target temperature can effectively improve laser ablation rate. Hai *et al.*[14] conducted laser ablation of molybdenum tungsten alloy at different sample temperatures, and their results showed that the ablation rate increased significantly with the increase of sample temperature. Wang *et al.*[15] simulated the thermal behaviors of Cu at different sample temperatures by using a one-dimensional heat transfer equation, finding that more substances were ablated as the Cu target was heated. Zou *et al.*[16] studied the ablation behavior at different matrix temperatures, finding that rising the matrix temperature will improve the ablation volumes.

Compared with nanosecond laser, femtosecond laser has the characteristic of high peak power, small heat-affected zone, and short pulse width.[17,18] The high peak power of a femtosecond laser acts on the surface of an object in a short period, instantly generating high energy that can change the absorption and motion of electrons. This is very different from the mechanism of conventional lasers such as nanosecond lasers that melt and vaporize materials by raising the local temperature of the workpiece. Therefore, femtosecond laser processing has become a non-hot-melt processing technology with ultra-high accuracy and ultra-high spatial resolution.[19,20] For femtosecond laser ablation, the pulse duration is less than the relaxation time between the electron and the lattice. In addition, due to the absence of heat loss in the femtosecond state, femtosecond laser occurs in the mechanism of "cold ablation".[21] Depending on the "thermal" properties of the nanosecond laser, preheating sample temperature (thermal ablation) increases the effectiveness of the ablation. However, femtosecond and nanosecond lasers have different energy deposition mechanisms. Furthermore, because of the "cold" nature of the femtosecond pulse, the effect of increasing target temperature on improving femtosecond laser ablation may or may not be small. After femtosecond laser irradiation, the target material exhibits a highly nonequilibrium state at two different temperatures of the electron system and the lattice system, and then reaches thermal equilibrium. Electron–lattice coupling is the main feature of femtosecond laser processing of target material. The theoretical research on femtosecond laser ablation at different sample temperatures is rare. Therefore, it is necessary to conduct theoretical and experimental research on femtosecond laser ablation after preheating the sample.

In this paper, experiments on and simulations of fem-

†Corresponding author. E-mail: amchen@jlu.edu.cn

‡Corresponding author. E-mail: mxjin@jlu.edu.cn

© 2024 Chinese Physical Society and IOP Publishing Ltd 

tosecond laser ablation processing of preheated metal samples are performed. In the experiments on femtosecond laser ablation of copper, the ablation depth is measured by confocal microscopy. Subsequently, the two-temperature model (TTM) is used to simulate the femtosecond single-pulse laser ablation of copper at different sample temperatures. Preheating is achieved by controlling the initial temperature of the sample. Once the lattice temperature exceeds the critical temperature ($0.9T_{\rm cr}$), the material is removed. The effect of sample temperature on the electron temperature and lattice temperature are analyzed and the ablation depth is simulated. Compared with the ablation depths, the simulation results are in general consistence with the trend of the experimental data. The results show that the sample temperature can improve the absorption rate of the target material, increase the optical penetration depth, and reduce the thermal diffusivity, thus improving the ablation rate of the material processed by femtosecond laser.

## 2. Model and computational setup

In the following are described the basic equations used to define the TTM model and the formulas used to calculate some important quantities that appear in the basic equations, including the laser source term, electron–lattice coupling factor, heat capacity and conductivity, and absorptivity and absorption coefficient. The last subsection provides some detailed information about the calculation configuration, such as the boundary and initial conditions, the axisymmetric model of laser ablation, and surface ablation.

### 2.1. Two-temperature model

Unlike the ablation process of traditional long-pulsed lasers, the ablation process that occurs in femtosecond laser processing cannot be directly characterized by a macroscopic heat exchange model.[22] During femtosecond laser ablation, heat is transferred to the lattice through electron–phonon collisions. According to Fourier's law of heat conduction, two equations for electron temperature and lattice temperature can be obtained, called TTM. For the two-dimensional case, the control equation is as follows:[23]

$$C_{\rm e}\frac{\partial T_{\rm e}}{\partial t}=\nabla\left(k_{\rm e}\nabla T_{\rm e}\right)-G(T_{\rm e}-T_{\rm l})+S(z,r,t), \tag{1}$$

$$C_{\rm l}\frac{\partial T_{\rm l}}{\partial t}=\nabla\left(k_{\rm l}\nabla T_{\rm l}\right)+G(T_{\rm e}-T_{\rm l}), \tag{2}$$

where $S(z,r,t)$ represents the absorbed laser heating source, $t$ is the time, $r$ is the distance from the observation point to the laser beam axis, $z$ is the penetration depth from the top surface, $C_{\rm e}$ and $k_{\rm e,}$ represent the heat capacity and thermal conductivity of the electron, and $C_{\rm l}$, and $k_{\rm l}$ denote the heat capacity and thermal conductivity of the lattice, $T_{\rm e}$ and $T_{\rm l}$ are the electron temperature and the lattice temperature, respectively, and $G$ is the electron–lattice coupling factor.

### 2.2. Laser source term

The intensity of a femtosecond laser follows a Gaussian distribution in both time and space. Assuming that the focus of the laser is located at $z=0$ on the surface of the workpiece. Considering the influence of free electron density, the laser intensity inside the material can be expressed as[24]

$$\begin{aligned}S(z,r,t) &= \frac{A(T_{\rm l})}{\delta+\delta_{\rm b}}\sqrt{\frac{4\ln 2}{\pi}}\frac{F}{\tau}\exp\left(-\frac{r^2}{r_0^2}\right)\\ &\quad\times\exp\left(4\ln 2\left(\frac{(t-2\tau)^2}{\tau^2}\right)\right)\exp\left(-\frac{z}{\delta+\delta_{\rm b}}\right),\end{aligned} \tag{3}$$

where $F$ is the laser fluence, $A(T_{\rm l})$ is the absorptivity of the material, $r$ is the beam radius at the laser focal plane, and $\tau$ is the pulse width. $\delta$ is the optical penetration depth for copper, with $1/b(T_{\rm l})$ taken herein, and $\delta_{\rm b}$ is the ballistic range of copper, taken as 105 nm.[25]

### 2.3. Electron–lattice coupling factor

The energy transfer rate between electron and lattice is constrained by electron–lattice coupling. For more accurate simulations, the model uses a dynamic electron–lattice coupling coefficient as follows:[26]

$$G=\begin{cases}0.56\times10^{17}, \quad \text{for } T_{\rm e}\le 2750\ \text{K},\\ 1.341\times10^{17}-1.407\times10^{14}T_{\rm e}\\ +5.988\times10^{10}T_{\rm e}^2-7.93\times10^{6}T_{\rm e}^3\\ +555.2T_{\rm e}^4-0.023272T_{\rm e}^5\\ +6.041\times10^{-7}T_{\rm e}^6-9.529\times10^{-12}T_{\rm e}^7\\ +8.377\times10^{-17}T_{\rm e}^8-3.15\times10^{-22}T_{\rm e}^9,\\ \text{for } 2750\ \text{K}\le T_{\rm e}\le 5\times10^4\ \text{K}.\end{cases} \tag{4}$$

### 2.4. Heat capacity and conductivity

Lin *et al.*[27] have obtained an expression of the electrical thermal capacity of copper as follows:

$$C_{\rm e}=\begin{cases}117.47T_{\rm e}, \quad \text{for } T_{\rm e}\le 2\times10^3\ \text{K},\\ -2.049\times10^4-26.64T_{\rm e}\\ +0.0996T_{\rm e}^2-1.122\times10^{-5}T_{\rm e}^3\\ +5.735\times10^{-10}T_{\rm e}^4-1.524\times10^{-14}T_{\rm e}^5\\ +2.044\times10^{-19}T_{\rm e}^6-1.094\times10^{-24}T_{\rm e}^7,\\ \text{for } 2\times10^3\ \text{K}\le T_{\rm e}\le 5\times10^4\ \text{K}.\end{cases} \tag{5}$$

Chen *et al.*[28] have developed an expression for electronic thermal conductivity as follows:

$$k_{\rm e}=\chi\frac{(v_{\rm e}^2+0.16)^{5/4}(v_{\rm e}^2+0.44)v_{\rm e}}{(v_{\rm e}^2+0.092)^{1/2}(v_{\rm e}^2+\eta v_1)}, \tag{6}$$

where $\chi$ and $\eta$ are the constants, $v_1 = T_l/T_F$, $v_e = T_e/T_F$, $T_F$ is the Fermi temperature. For copper, $T_F = 8.16 \times 10^{14}$ K, $\chi = 377$ W·m$^{-1}$·K$^{-1}$, and $\eta = 0.319$.

The lattice heat capacity used in the simulation experiment is[26]

$$C_l = 313.7 + 0.324T_l - 2.687 \times 10^{-4}T_l^2 + 1.257 \times 10^{-7}T_l^3. \quad (7)$$

The thermal conductivity of metal lattice is much lower than that of electrons. Usually, free electrons dominate the thermal conduction process, and the lattice thermal conductivity is taken as 1% of the thermal conductivity $k_{eq}$.[29] The expression of $k_{eq}$ is[26]

$$k_{eq} = 407.9 - 0.0272T_l - 2.658\times10^{-5}T_l^2 - 3.0\times10^{-9}T_l^3. \quad (8)$$

### 2.5. Absorptivity and absorption coefficient

Under the same laser irradiation, the surface temperature is one of the most important parameters. Ignoring other effects, the energy absorbed by the sample surface depends only on the laser fluence and the absorptivity and absorption coefficient of the sample. In an ideal vacuum environment, the single wavelength absorptivity of copper can be calculated from the Hagen–Rubens equation[30,31]

$$A(T_l) = 2\sqrt{\frac{2\omega\varepsilon_0}{\sigma}} = (8\varepsilon_0\omega\Omega(T_l))^{1/2}. \quad (9)$$

The absorption coefficient is expressed as[31]

$$b(T_l) = \sqrt{\frac{4\pi\sigma}{\varepsilon_0\lambda c}} = \sqrt{\frac{4\pi}{\varepsilon_0\lambda c\Omega(T_l)}}, \quad (10)$$

where $A(T_l)$ denotes the absorptivity, $b(T_l)$ represents the absorption coefficient, and $\Omega(T_l)$ refers to the metal resistively, which is a function of temperature. The dielectric constant $\varepsilon$ in vacuum is a constant, and $\varepsilon = 8.85 \times 10^{-12}$ F/m. In Eq. (9) $\omega = 2\pi c/\lambda$, with $c$ being the speed of light in vacuum and $\lambda$ being the laser wavelength. The absorptivity and absorption coefficient of copper at temperature $T_l$ are approximated expressed as

$$A(T_l) = 408.54\sqrt{\Omega(T_l)}, \quad (11)$$

$$b(T_l) = \frac{5.916 \times 10^4}{\sqrt{\Omega(T_l)}}. \quad (12)$$

Metal resistance makes an important contribution to laser absorption, and the metal resistively of copper varies with the surface temperature of the target[30]

$$\Omega(T_l) = \begin{cases} 10^{-8}\left(-0.125 + 0.675 \times 10^{-2}T\right), & \text{for } 273.15\ \text{K} \le T_l \le 1358\ \text{K}, \\ 10^{-8}\left(6.2 + 1.02 \times 10^{-2}T\right), & \text{for } 1358\ \text{K} \le T_l \le 2835\ \text{K}. \end{cases} \quad (13)$$

The Hagen–Rubens formula for laser absorption, which is commonly used as a resistance function, is used for the absorption of metals in 800-nm-wavelength laser. The absorptivity and absorption coefficient of metal to 800-nm laser can be expressed as

$$A(T_l) = \begin{cases} 408.54 \times 10^{-4}\sqrt{-0.125 + 0.675 \times 10^{-2}T_l}, & \text{for } 273.15\ \text{K} \le T_l \le 1358\ \text{K}, \\ 408.54 \times 10^{-4}\sqrt{6.2 + 1.02 \times 10^{-2}T_l}, & \text{for } 1358\ \text{K} \le T_l \le 2835\ \text{K}, \end{cases} \quad (14)$$

$$b(T_l) = \begin{cases} \dfrac{5.916 \times 10^8}{\sqrt{-0.125 + 0.675 \times 10^{-2}T_l}}, & \text{for } 273.15\ \text{K} \le T_l \le 1358\ \text{K}, \\ \dfrac{5.916 \times 10^8}{\sqrt{6.2 + 1.02 \times 10^{-2}T_l}}, & \text{for } 1358\ \text{K} \le T_l \le 2835\ \text{K}. \end{cases} \quad (15)$$

### 2.6. Boundary and initial conditions

According to the heat source term in the transient heat transfer equation, boundary conditions and heat flow functions must be set at the boundary of a specific system to constrain the heat transfer relationship between the heat transfer system and the external environment. The boundary conditions are set as follows:

$$\left.\frac{\partial T_{e,l}}{\partial n}\right|_{r=100\ \mu\text{m}} = 0, \quad (16)$$

$$\left.\frac{\partial T_{e,l}}{\partial n}\right|_{z=50\ \mu\text{m}} = 0. \quad (17)$$

According to Eq. (3), the peak of a single Gaussian laser pulse reaches the film surface when $t = 2\tau$. The initial conditions for $T_e$ and $T_l$ are[32]

$$T_e(z,r,0) = T_l(z,r,0) = T, \quad (18)$$

where $T$ is the initial sample temperature.

### 2.7. Axisymmetric model of laser ablation

Due to the rotational symmetry of laser ablation, a two-dimensional finite element model is established. Meanwhile, in order to simplify the calculation, geometric symmetry related to the central axis of the laser beam is also adopted. The

computational domain is 100 μm in the radial direction and 50 μm in the axial direction, representing the right half of the target material as shown in Fig. 1. The mesh refinement is performed on the laser beam in the axial direction.

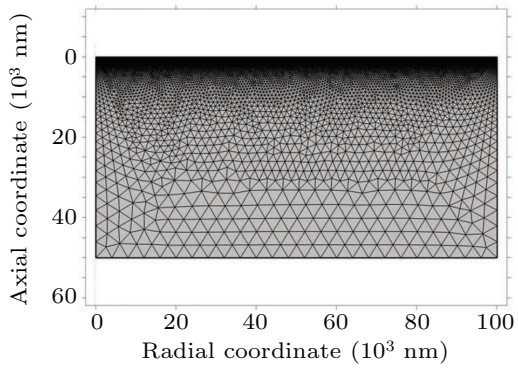



**Fig. 1.** Schematic diagram of the mesh profile.

### 2.8. Surface ablation

When the surface ablation is involved, the removed nodes caused by femtosecond laser ablation are removed from the calculation results. The result shows the existence of the isotherm and it is set to fill only the part with $T_l < 0.9T_{cr}$ so as to obtain the expected ablation results at the corresponding laser energy. Therefore, once the lattice temperature is 0.9 times higher than the thermodynamic critical temperature of the copper ($T_{cr} = 7696$ K) at the ablation temperature, ablation is triggered off and the material region above the ablation temperature is removed.[33,34] As a result, the contour of the ablation crater is obtained.

## 3. Experiment setup

Figure 2 shows the experimental setup of femtosecond laser ablation of copper. In this experiment, a regeneration amplified Ti:sapphire laser system (Libra, Coherent) is used to deliver a laser beam with a pulse width of 50 fs and wavelength of 800 nm. The laser system operating in single shot mode is fired by sending a command ('man:trig') to the serial port (RS232) of the synchronization and delay generator (SDG). The corresponding controlled repetition ratio of the femtosecond laser is approximately 1 Hz. By adjusting the compression grating, it is ensured that the laser pulse duration is 50 fs. A halfwave plate and a Glan laser polarizer allowed for the adjustment of laser energy. The laser beam is focused onto the surface of the sample through the focal length lens L, and copper adheres to the heating table through the thermally conductive adhesive. The heating table is fixed on a three-dimensional translation stage, and its movement is controlled by computer programming. A constant temperature-heating table is used to heat the sample. All measurements are conducted in the air.

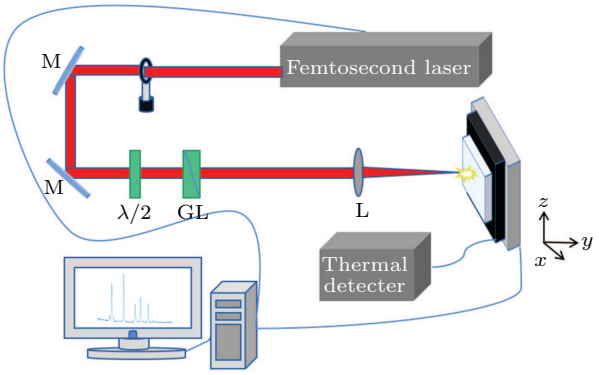



**Fig. 2.** Diagram of the experimental setup.

## 4. Results and discussion

In this section, the established model is verified by comparing the calculated ablation depth with the experimentally measured ablation depth. The influence of sample temperature on ablation depth, electron and lattice temperature under single pulse are analyzed.

### 4.1. Experimental ablation depth and model verification

We use confocal microscopy to measure the morphologies and ablation depths of experimental samples. Confocal microscopy technology is a high-resolution imaging technique in which the sample surface is scanned by a laser scanning system, and the laser light and reflected light are focused on the same plane through using the confocal technique to obtain clear, high-quality images. Figures 3(a) and 3(b) show the corresponding experimental results for multi-pulse ablation with 100 pulses and 200 pulses, respectively. With the help of confocal laser scanning microscope software, the ablation crater cross-section profile is obtained as shown in Fig. 3(c). The 22-μm-deep blation craters are obtained at 100 pulses and 40 μm-deep blation craters at 200 pulses.

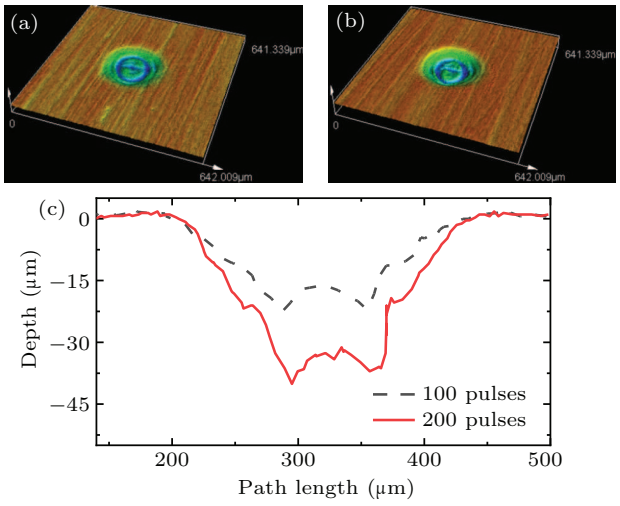



**Fig. 3.** Morphologies of laser ablation at (a) 100 and (b) 200 pulses, and comparison of cross-sectional profiles (c) at 100 and 200 pulses. Laser width is 50 fs, wavelength is 800 nm, energy is 50.5 J/cm$^2$, and sample temperature is 303 K.

We determine the variations of average ablation depth of each pulse with the ablation depth of a single pulse by using multi-pulse ablation. Figure 4 shows the single-pulse ablation depths versus sample temperature for 100 pulses and 200 pulses. Two different numbers of pulses are chosen in the figure. As can be seen, the single-pulse ablation depths for 100 and 200 pulses are very consistent. This result indicates that the number of pulses hardly affects the average value of ablation depth. The laser operates in a single-shot mode with no heat accumulation effect. Every time the laser irradiates the sample, the temperature of the sample will quickly return to the ambient temperature. The heat generated by the previous pulse does not accumulate on the material to be irradiated by the next laser. The single-pulse ablation depths for 100 and 200 pulses in Fig. 4 change with sample temperature. It may be that the energy reaches the sample surface unequally at different substrate temperatures during the experiment, and the energy loss will be different, which in turn will affect the result of ablation depth. The ablation depth is measured by laser scanning confocal microscopy on the outline of the crater. The ablation depth is the thickness of the metal film in the portion of the target material irradiated by the laser where the phase explosion occurs.

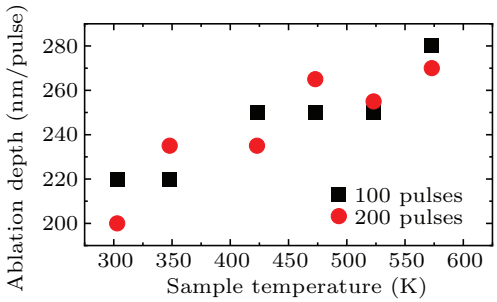



**Fig. 4.** Variations of ablation depth of single-pulse with sample temperature for different pulses.

To obtain a more accurate single-pulse femtosecond laser ablation depth, the square dots in Fig. 5 show the average ablation depth. When a laser irradiates the metal target at high temperatures, due to the interaction between the laser and the molecules and atoms (ions) in the target, the target will absorb more laser energy and be heated. The result indicates that under a certain laser irradiation intensity, the higher the sample temperature, the higher the ablation efficiency is.

The ablation crater depths at different sample temperatures are shown in Fig. 5. The phase explosion mechanism determines the ablation pattern of the metal in the higher region of the sample temperature. As shown in Fig. 5, the simulated depth increases from 221.4 nm to 261.1 nm as the sample temperature increases from 303 K to 603 K, and the experimental ablation depth continues to increase from 210 nm to 275 nm. Some interesting observations of the ablation depth can be noted. The measured ablation depths are slightly overestimated compared with the simulated values in the sample temperature range of 303 K–423 K and slightly underestimated in the higher sample temperature range ($\geq$ 423 K). An ablation depth is measured to be 242.5 nm for an energy density at 423 K, and a simulated ablation depth is obtained to be 239.9 nm. Theoretical trend and experimental trend are the identical. However, the ablation depth is a few nanometers greater than the simulated depth. In the higher temperature region, the phase explosion mechanism exhibits high uncertainty in simulation results and experimental results. Unlike the simulation results, multiple femtosecond laser irradiations are used in the experiments to measure the ablation depth, which may change,[35] and the measurement equipment during the experiments may also affect the results. The reason for the error could also be that the loss of laser energy is neglected during the calculation of the theoretical values and that the energy reaching the sample surface is assumed to be equal for different substrate temperatures during the experiments. The experimental errors can be minimized by taking the average of the ablation depths. In general, the simulated and experimental temperature-dependent ablation depths are similar to each other essentially.

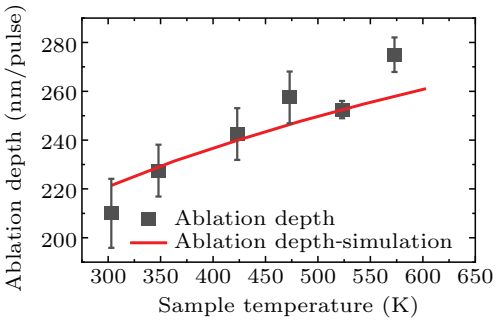



**Fig. 5.** The simulated and measured variations of single-pulse ablation depth with sample temperature under irradiation of laser with width 50 fs, wavelength 800 nm, and fluence 50.5 J/cm$^2$.

### 4.2. Effect of sample temperature on ablation crater

The two-dimensional images of copper ablation at a laser fluence of 10 J/cm$^2$ and a pulse width of 50 fs are shown in Figs. 6(a) and 6(b). As can be seen from Fig. 6(a), at a sample temperature of 300 K, a crater with a depth of 39.0 nm and a radius of 17.8 μm is created. When the sample temperature is 600 K, single pulse irradiation is applied to the sample, a crater with a depth of 81.4 nm and a radius of 31.1 μm is shown in Fig. 6(b). The two-dimensional images of copper ablation at a laser parameter of 40 J/cm$^2$ and a pulse width of 50 fs are shown in Figs. 6(c) and 6(d). When the sample temperature is 300 K, a crater with a depth of 195.5 nm and a radius of 54.1 μm is created in Fig. 7(c). When the sample temperature is 600 K, a crater with a depth of 235.2 nm and a radius of 59.7 μm is created in Fig. 6(d). As the sample temperature rises, the depth of the crater deepens and the radius of the crater significantly increases. At high sample temperature the ablation depth and ablation radius can be higher than those at room temperature under the same incident laser energy. Therefore, there is a heat accumulation between the laser ablation and increasing the sample temperature.

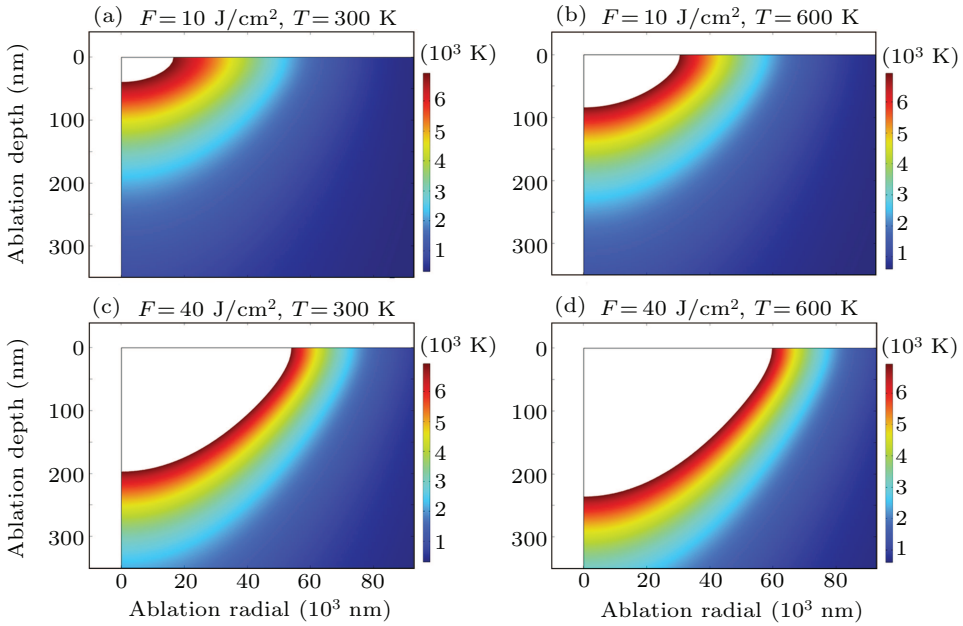



**Fig. 6.** Two-dimensional images of single pulse femtosecond laser ablation crater under simulation.

The simulation results in Figs. 7(a) and 7(b) respectively show the influences of sample temperature on the depth and radius of copper ablation under a single pulse. The results indicate that the ablation depth and radius significantly grow with the increase of sample temperature, which is because of the decrease in ablation threshold. At the same sample temperature, the ablation depth and radius mainly depend on the laser fluence.

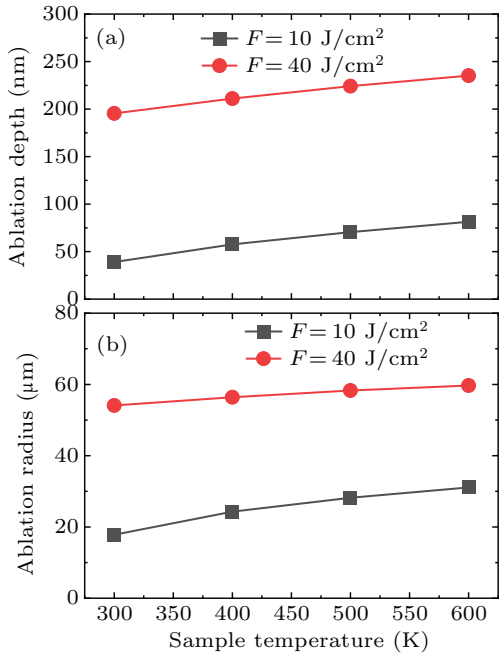



**Fig. 7.** Variations of (a) ablation depth and (b) ablation radius with sample temperature under different laser fluences.

### 4.3. Effect of sample temperature on electron temperature and lattice temperature

The relationship among the electron temperature, lattice temperature, and sample temperature of ablated copper is shown in Fig. 8. The sample temperature affects not only the peak temperature of electrons and relaxation time required to reach the equilibrium state, but also the lattice temperature and the final temperature after the electrons have reached equilibrium with the lattice. As shown in Fig. 8, since the time scale of electron energy absorption is on the order of femtoseconds, when the laser energy is deposited, the electrons are heated, and the electron temperature rises sharply to a peak that is far greater than the lattice temperature. The sample temperature in a range from 300 K to 600 K is used for simulation research. With the increase of sample temperature, the maximum value of the electron temperature rises. At the same time, the electron temperature increases after it has reached equilibrium, and the relaxation time required to reach the equilibrium state also becomes longer. The lattice temperature rises rapidly, and after reaching the equilibrium temperature, it

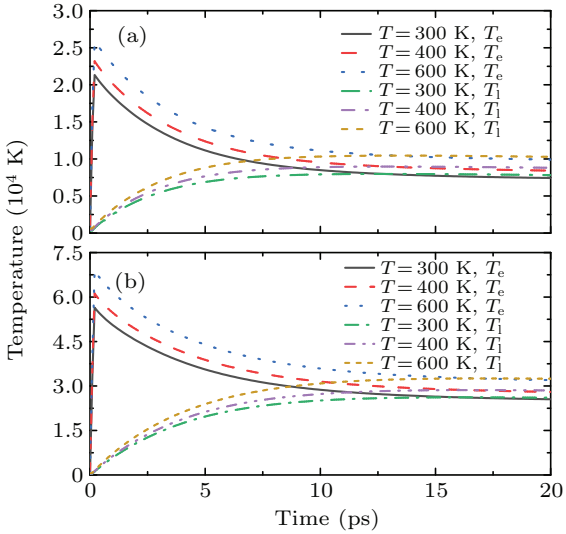



**Fig. 8.** Electron and lattice temperatures at different sample temperatures, with laser fluences being (a) 10 J/cm$^2$ and (b) 40 J/cm$^2$.

begins to keep relatively stable. It can be seen that the higher the sample temperature, the faster the lattice temperature rises and the shorter the time required the material to reach the critical temperature ($0.9T_{cr}$). Therefore, preheating the sample can effectively perform laser processing.

### 4.4. Effect of sample temperature on radial and axial lattice temperatures

When the sample temperatures are 300 K and 600 K, the lattice temperature distribution of the ablated crater is obtained as shown in Fig. 6. It can be observed that the lattice temperature gradually decreases along the axial direction and radial direction, indicating that the sample temperature has a small thermal influence on the processing process and has little effect on the surrounding area of the ablated material.

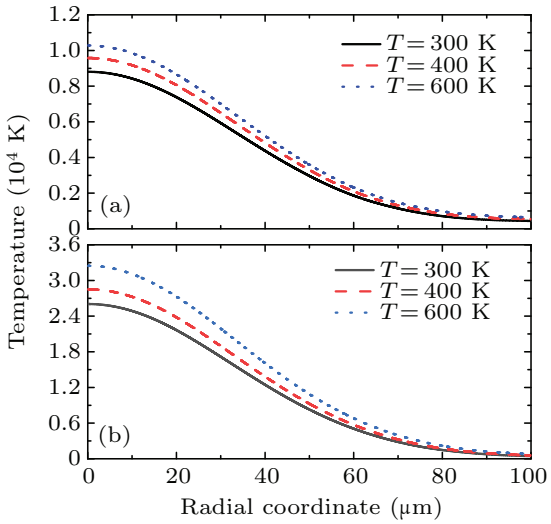



**Fig. 9.** Lattice temperature distribution along radial direction at different sample temperatures, with laser fluences being (a) 10 J/cm$^2$ and (b) 40 J/cm$^2$.

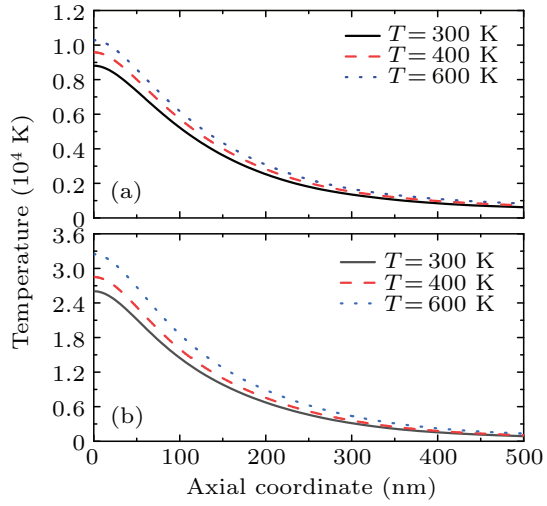



**Fig. 10.** Lattice temperature distribution in axial direction at different sample temperatures, with laser fluences being (a) 10 J/cm$^2$ and (b) 40 J/cm$^2$.

By selecting different sample temperatures, the radial lattice temperature distribution and the axial lattice temperature distribution of copper are obtained, and the results are shown in Figs. 9 and 10, respectively. As shown in Fig. 9, the maximum lattice temperature of the target surface significantly increases with the sample temperature rising. The temperature of each point in the radial position increases with the sample temperature increasing, which is determined mainly by the thermal accumulation effect of sample preheating. Figure 10 shows the rapid decrease of temperature in the thin layer of the copper surface layer. As the sample temperature increases, the lattice temperature of each point in the axial direction increases. This is due to the heat accumulation effect of sample preheating. Preheating the sample can effectively increase the radial lattice temperature and the axial lattice temperature, thus making it easier for the target to reach the removal temperature point.

### 4.5. Effect of sample temperature on maximum lattice temperature of target surface

The model uses the absorptivity and absorption coefficient of the target to express the laser utilization rate. It is indicated that the absorptivity and absorption coefficient are temperature dependent as expressed in Eqs. (14) and (15). Therefore, the higher the temperature, the greater the absorptivity, the smaller the absorption coefficient, and the higher the laser utilization rate.

In order to study the influence of preheating temperature on the temperature rise of the target, the maximum lattice temperature of the copper surface is extracted. The relationship between the sample temperature and the maximum lattice temperature of the copper surface is shown in Fig. 11. The upward trend of temperature is consistent with the change trend of absorptivity of the target. It can be concluded that preheating is not a simple temperature superposition between the sample temperature and the temperature of femtosecond laser ablation, but a heat accumulation effect that increases the target temperature through preheating, leading to the increase of the target surface absorptivity and optical penetration depth. The higher the sample temperature, the higher the absorption rate of the target is. This can better improve the energy utilization rate of subsequent femtosecond laser and increase the temperature of the metal target. The target surface quickly reaches the critical temperature, the laser induced damage effect increases and thereby the ablation efficiency is improved.

There are many potential reasons that can affect the ablation rate and quality. Ujihara[36] calculated the surface reflectances of metals (aluminum, copper, sodium, potassium, silver, and gold) as a function of temperature. The calculation results indicate that the surface reflectance of the sample decreases with temperature increasing. On the contrary,

the surface absorption rate of the sample increases. The increase of sample temperature accelerates the movement speed of free electrons. The collision between free electrons and lattice becomes more frequent. It hinders the directional movements of free electrons in metal materials. This leads to an increase in the resistivity of metal materials as shown in Eq. (12). For higher sample temperatures, the lattice temperature (see Fig. 11) increases, owing to the increase of metal surface absorption rate. In addition, the thermal conductivity of metal is affected by temperature.[37] Two parts in metal material play a role in generating thermal conductivity. One part is the energy exchange between free electrons through collisions at different temperatures, and the other part is the temperature transferring from the lattice through different vibration frequencies. The ablation threshold is also a factor affecting femtosecond laser ablation. Thorstensen and Foss[38] studied the effect of substrate temperature on the ablation threshold, and their results show that an increase in target temperature results in a lower ablation threshold and weaker lattice bonding.

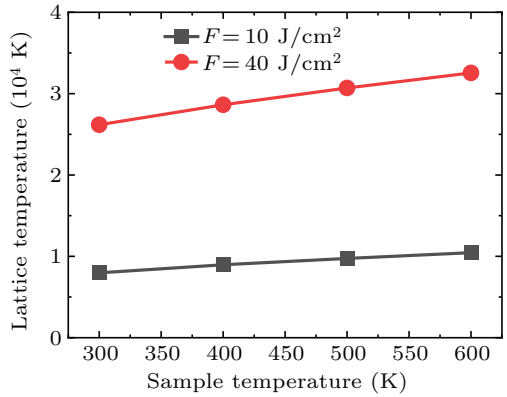



**Fig. 11.** Variations of maximum lattice temperature with sample temperature at $F = 10$ J/cm$^2$ and 40 J/cm$^2$.

Increasing the sample temperature can enhance the ablation rate. Preheating the ablation target increases the initial energy on the target surface, which means that more initial energy is available for femtosecond laser ablation of the metal. The thermal decomposition of the hot sample requires less laser energy, which increases the laser ablation rate by 30%.[39] Therefore, increasing the sample temperature is a more effective way to increase the ablation rate. These results are in agreement with the present simulations (see Fig. 4). Thus, we can confirm that this method allows a better coupling between sample and laser pulse, producing a higher ablation quality.

## 5. Conclusions

In this work, we conducted the simulation of and the experiment on the characteristics of copper ablated by femtosecond laser at different sample temperatures. The ablation depth of copper is measured by using confocal microscopy. The single-pulse femtosecond laser ablation of copper is simulated by using the TTM. The simulation results show that increasing the sample temperature can improve the utilization of laser energy and enhance the ablation effect. The comparison between the experimental results and the simulation results shows that they are well consistent in the ablation depth. The enhancing effects of sample temperature on the electron temperature and lattice temperature are analyzed. Therefore, preheating the sample can improve femtosecond processing efficiency. This work provides some rules to explain the temperature rise and ablation depth changes caused by femtosecond laser at different sample temperatures. In addition, an extended TTM model considering hydrodynamic effects will be further developed to help better understand the ablation characteristics of femtosecond laser at different sample temperatures.

## Acknowledgements

Project supported by the National Key Research and Development Program of China (Grant No. 2019YFA0307701) and the National Natural Science Foundation of China (Grant Nos. 11674128, 11674124, and 11974138).

## References

[1] Bykovskii N E, Zavedeev E V and Senatskii Y V 2015 *Phys. Solid State* **57** 798
[2] Andre P, Abbaoui M, Augeard A, Desprez P and Singo T 2016 *Plasma Chem. Plasma Process.* **36** 1161
[3] Bykovsky N E, Zavedeev E V, Ralchenko V G and Senatsky Y V 2015 *Laser Phys. Lett.* **12** 056102
[4] Tarek E, Mostafa W Z, Allam R, El-Samanoudy S I and Saadi D G 2022 *Lasers Surg. Med.* **54** 237
[5] Chung I Y, Kim J D and Kang K H 2009 *Int. J. Precis. Eng. Man.* **10** 11
[6] Yu H, Li H, Wang Y, Cui L, Liu S and Yang J 2018 *Opt. Laser Technol.* **100** 57
[7] Liu L, Morgan S P, Correia R and Korposh S 2022 *Opt. Laser Technol.* **147** 107696
[8] Momeni A and Mahdieh M H 2015 *Laser Phys. Lett.* **12** 076102
[9] Zhou R, Lin S, Ding Y, Yang H, Keng K O Y and Hong M 2018 *Opto-Electron. Adv.* **1** 180014
[10] Singh K S and Sharma A K 2017 *J. Vac. Sci. Technol. A* **35** 031305
[11] Farrokhi H, Gruzdev V, Zheng H and Zhou W 2019 *J. Opt. Soc. Am. B* **36** 1091
[12] Sangines R, Sobral H and Alvarez-Zauco E 2012 *Appl. Phys. B* **108** 867
[13] Tavassoli S H and Khalaji M 2008 *J. Appl. Phys.* **103** 83118
[14] Hai R, He Z, Wu D, Tong W, Sattar H, Imran M and Ding H 2019 *J. Anal. At. Spectrom.* **34** 2378
[15] Wang Y, Wang Q, Chen A and Jin M 2021 *Optik* **230** 166338
[16] Zou Q, Li C, Ding Z, Bao Z, Zhang T, Zhang Q, Zhang L and Bi Y 2023 *J. Anal. At. Spectrom.* **38** 429
[17] Tsai Y H, Chen B C, Ho C Y, Chiou Y J, Chen K H, Chen C S and Wen M Y 2017 *Ceram. Int.* **43** S573
[18] Koritsoglou O, Loison D, Uteza O and Mouskeftaras A 2022 *Opt. Express* **30** 37407
[19] Chen M, He T and Zhao Y 2022 *Opt. Laser Technol.* **147** 107628
[20] Ionin A A, Kudryashov S I, Seleznev L V, Sinitsyn D V, Bunkin A F, Lednev V N and Pershin S M 2013 *J. Exp. Theor. Phys.* **116** 347

[21] Mirza I, Bulgakova N M, Tomastik J, Michalek V, Haderka O, Fekete L and Mocek T 2016 *Sci. Rep.* **6** 39133

[22] Chen C, Zhang F, Zhang Y, Xiong X, Ju B F, Cui H and Chen Y L 2022 *Appl. Surf. Sci.* **576** 151722

[23] Chen J K, Latham W P and Beraun J E 2002 *Numer. Heat Transfer, Part B* **42** 1

[24] Wang M, Mei W and Wang Y 2019 *Opt. Laser Technol.* **113** 123

[25] Xue N, Ren Y, Ren X, Ren N, Lin Q, Wang Q and Qin K 2018 *Comput. Mater. Sci.* **148** 60

[26] Ren Y, Chen J and Zhang Y 2011 *J. Appl. Phys.* **110** 113102

[27] Lin Z, Zhigilei L V and Celli V 2008 *Phys. Rev. B* **77** 075133

[28] Chen J K, Tzou D Y and Beraun J E 2006 *Int. J. Heat Mass Transfer* **49** 307

[29] Klemens P G and Williams R K 1986 *Int. Mater. Rev.* **31** 197

[30] Xie J, Kar A, Rothenflue J A and Latham W P 1997 *J. Laser Appl.* **9** 77

[31] Li L, Zhang D, Li Z, Guan L, Tan X, Fang R, Hu D and Liu G 2006 *Physica B* **383** 194

[32] Hu H, Ji Y, Hu Y, Ding X, Liu X, Guo J H, Wang X L and Zhai H 2011 *Chin. Phys. B* **20** 44204

[33] Dong Y, Wu Z, You Y, Yin C and Li X 2019 *Opt. Mater. Express* **9** 4194

[34] Ren Y, Cheng C W, Chen J K, Zhang Y and Tzou D Y 2013 *Int. J. Therm. Sci.* **70** 32

[35] Wu Z, Zhang N, Zhu X, An L, Wang G and Tan M 2018 *Chin. Phys. B* **27** 077901

[36] Ujihara K 1972 *J. Appl. Phys.* **43** 2376

[37] Li Y, Li W, Han T, Zheng X, Li J, Li B, Fan S and Qiu C W 2021 *Nat. Rev. Mater.* **6** 488

[38] Thorstensen J and Foss S E 2012 *J. Appl. Phys.* **112** 2248

[39] Zemaitis A, Miksys J, Gaidys M, Gecys P and Gedvilas M 2019 *Mater. Res. Express* **6** 065309